High-efficiency electrosynthesis of urea over bacterial cellulose regulated Pd–Cu bimetallic catalyst†

Shengbo Zhang,‡[ab] Jing Geng,‡[ab] Zhong Zhao,[ab] Meng Jin,[ab] Wenyi Li,[ab] Yixing Ye,[ab] Ke Li,*[c] Guozhong Wang, [iD][ab] Yunxia Zhang, [iD][ab] Huajie Yin, [iD][ab] Haimin Zhang [iD] *[ab] and Huijun Zhao [iD][d]

Ambient synthesis of urea through electrocatalytic coupling reaction of carbon dioxide (CO_2) with nitrate (NO_3^-) has been regarded as a promising means to substitute the industrial energy- and capital-concentrated Haber–Bosch and Bosch–Meiser processes. Here we report the fabrication of PdCu alloying nanoparticles (NPs) anchored on carbonized bacterial cellulose (CBC) (PdCu/CBC) for ambient electrosynthesis of urea. As the electrocatalyst, the PdCu/CBC exhibits superior electrocatalytic activity toward urea synthesis with CO_2 and NO_3^-, affording a remarkable urea yield rate of 763.8 ± 42.8 µg h^{-1} $mg_{cat.}^{-1}$ at −0.50 V (*vs.* RHE) and an exceptional faradaic efficiency (FE) of 69.1 ± 3.8% at −0.40 V (*vs.* RHE) under ambient conditions. The theoretical calculations unveil that this alloying catalyst provides Pd and Cu dual active sites with favored internal electron transferability, enabling generation of key $*NO_2$ and $*CO_2$ intermediates to facilitate C–N coupling reaction for urea synthesis. The *operando* spectroscopy characterization studies support the theoretical calculation results. To ensure the accuracy of the analysis data in this work, we investigated in detail the influence of the by-products in urea synthesis on the diacetyl monoxime colorimetric method and ^1H nuclear magnetic resonance method for urea quantitative determination.

Broader context

Urea is one of the most essential nitrogen-based fertilizers in agricultural production and other chemical synthesis with an output of ~100 million tons per year. Currently, the industrial synthesis of urea is highly dependent on the traditional Haber–Bosch and Bosch–Meiser processes under harsh reaction conditions. Recent studies have demonstrated that the electrocatalytic coupling of N_2 with CO_2 provides the feasibility for direct urea production under ambient conditions. Despite some achievements, the urea yield rate and faradaic efficiency are still very low, due to the high N≡N bond energy, very low N_2 solubility in aqueous electrolyte, and competitive N_2 hydrogenation and CO_2 hydrogenation reactions and so on. The coupling of CO_2 and NO_3^- (or NO_2^-) in electrocatalysis could be an effective means to solve the above issues and realize high-efficiency urea production with high current efficiency. Herein, we reported an adsorption-regulated synthetic approach utilizing bacterial cellulose as the adsorption regulator to fabricate a Pd–Cu bimetallic catalyst, which as an electrocatalyst exhibited superior electrocatalytic C–N coupling activity toward urea production with a very high faradaic efficiency of 69.1 ± 3.8% at −0.40 V (*vs.* RHE), surpassing almost all of the currently reported urea synthesis electrocatalysts. To ensure the accuracy of the analysis data in this work, we investigated in detail the influence of the by-products in urea synthesis on the diacetyl monoxime colorimetric method and ^1H NMR method for urea determination.

[a] *Key Laboratory of Materials Physics, Centre for Environmental and Energy Nanomaterials, Anhui Key Laboratory of Nanomaterials and Nanotechnology, CAS Center for Excellence in Nanoscience, Institute of Solid State Physics, Chinese Academy of Sciences, Hefei 230031, China. E-mail: zhanghm@issp.ac.cn*

[b] *University of Science and Technology of China, Hefei 230026, China*

[c] *Key Laboratory of Agricultural Sensors, Ministry of Agriculture, School of Information and Computer, Anhui Agricultural University, Hefei 230026, China. E-mail: kelee@ustc.edu.cn*

[d] *Center for Catalysis and Clean Energy, Griffith University, Gold Coast Campus, QLD4222, Australia*

Introduction

Urea (NH_2CONH_2) is not only the most widely utilized nitrogen fertilizer in agriculture, but also serves as the critical feedstock to produce fine chemicals such as urea-formaldehyde and barbiturates in chemical synthesis.[1,2] Currently, the industrial synthesis of urea is highly dependent on the energy- and capital-concentrated Haber–Bosch and Bosch–Meiser processes, namely, through $N_2 + 6H^+ + 6e^- \rightarrow 2NH_3$ and $2NH_3 + CO_2 \rightarrow NH_2CONH_2 + H_2O$ reactions under extreme conditions.[3,4] These two processes for urea production not only consume enormous fossil energy, but also produce huge emissions of CO_2.[5–7] Undoubtedly, the exploration of renewable-energy-driven new techniques for urea production is highly needed for the sustainable development of our society.

Recently reported studies have demonstrated that the electrochemical synthesis of urea under ambient conditions through an electrocatalytic coupling reaction of carbon dioxide (CO_2) with nitrogen-containing precursors (e.g., N_2, NO, NO_3^-, NO_2^-) has been widely accepted as a promising approach to substitute the industrial urea production process.[8–29] At the beginning, the electrocatalytic coupling of N_2 with CO_2 was first investigated on Pd_1Cu_1/TiO_2-400 and Bi–$BiVO_4$ catalysts for urea synthesis under ambient conditions.[9,10] In their studies, N_2 can be effectively adsorbed and activated to generate $*N_2$ intermediates, which promote CO_2 reduction to form $*CO$, and then the generated $*CO$ further reacts with $*N_2$ to produce the desirable $*NCON*$ intermediates via a thermodynamically feasible electrochemical C–N coupling reaction.[9,10] Despite some achievements, the electrocatalytic urea synthesis performance is still low (urea yield rate <6.0 mmol h^{-1} g^{-1}, faradaic efficiency $<13\%$) in a N_2-incorporated reaction system, mainly owing to the high bond energy of $N\equiv N$ without dipole, the low solubility of N_2 in aqueous electrolyte, and the competitive hydrogen evolution reaction (HER).[9,10,30] To solve these issues caused by the N_2 precursor, nitrate (NO_3^-) and nitrite (NO_2^-) in aqueous electrolytes have been investigated as the nitrogen sources coupling with CO_2 for electrocatalytic synthesis of urea under ambient conditions.[16–28] In comparison with the N_2 reactant, the superiorities of NO_3^- and NO_2^- as the reactants are their high solubility in aqueous solution and the lower dissociation energy of the $N=O$ bond (204 kJ mol^{-1}), which enable more efficient C–N coupling reaction for urea production.[16–28] Besides this, the development of high-efficiency electrocatalysts is also critically important for urea synthesis. To date, precious and non-precious metal based electrocatalysts have been fabricated and investigated for electrocatalytic coupling of NO_3^- and NO_2^- (or NO) and CO_2 to efficiently synthesize urea under ambient conditions, exhibiting high electrocatalytic activities.[16–29] In terms of catalytic mechanistic research, Zhang et al. reported that the formation of $*CO$ and $*NH_2$ intermediates through the adsorption and activation of CO_2 and NO on a Zn nanobelt catalyst is critically important for subsequent C–N coupling synthesis of urea with a yield rate of 15.13 mmol h^{-1} g^{-1} and a faradaic efficiency of 11.26% at ~ 40 mA cm^{-2}.[29] Meanwhile, Zhang et al. synthesized urea by coupling CO_2 with NO_2^- on oxygen vacancy-rich ZnO porous nanosheets with a yield rate of 16.56 µmol h^{-1} and a faradaic efficiency of 23.26% at -0.79 V (vs. RHE).[26] Yu et al. revealed that the key steps during electrocatalytic urea synthesis are the generation of $*NO_2$ and $*CO_2$ intermediates through the adsorption and activation of CO_2 and NO_3^- on $In(OH)_3$ with exposed {100} facets and InOOH with oxygen vacancies.[17,18] Recently, Rose Amal and co-workers reported a single-atom electrocatalyst with Cu–N_4 sites to couple CO_2 and NO_3^- with a urea yield rate of 4.3 mmol s^{-1} cm^{-2} and a faradaic efficiency (FE) of 28% at -0.9 V (vs. RHE).[22] On the basis of these reported works, it can be concluded that design and construction of dual active sites in an electrocatalyst are highly desirable for high-efficiency generation of CO_2 and NO_3^- (or NO_2^-) derived active intermediates to synthesize urea under ambient conditions.

Herein, bacterial cellulose (BC) was used as the adsorption regulator to fabricate PdCu alloying nanoparticles anchored on the carbonized BC (PdCu/CBC). The as-synthesized PdCu/CBC shows a Pd to Cu molar ratio of 1 : 1 and a surface area of 162.4 m^2 g^{-1} with microporous and mesoporous structures. In the presence of CO_2 and NO_3^-, the PdCu/CBC as the electrocatalyst exhibits superior electrocatalytic activity toward urea synthesis with a remarkable urea yield rate of 763.8 $\pm$ 42.8 µg h^{-1} $mg_{cat.}^{-1}$ and a faradaic efficiency (FE) of 59.7 $\pm$ 3.4% at -0.50 V (vs. RHE) under ambient conditions. The high urea synthesis performance can be ascribed to PdCu alloying catalysts with favored internal electron transfer properties, simultaneously providing Pd and Cu dual active sites for the adsorption and activation of CO_2 and NO_3^- to generate their corresponding active intermediates for facilitating C–N coupling reaction, confirmed by the theoretical and experimental results. The findings in this work would be helpful for the design and development of high-efficiency electrocatalysts for electrochemical C–N coupling to synthesize urea.

Results and discussion

In this work, bacterial cellulose (BC) was used as the adsorption regulator to synthesize PdCu alloying nanoparticles anchored on carbonized bacterial cellulose (CBC) (denoted PdCu/CBC) by a synthetic approach combining wet-chemistry impregnation with a carbonization fixation process (Fig. S1, ESI†).[31,32] The pre-treated BC with rich oxygen groups (Fig. 1a) was used as the adsorption regulator to controllably impregnate Pd^{2+}/Cu^{2+} ions. The scanning electron microscopy (SEM) image in Fig. 1b showed the maintenance of the fiber-like carbon structure of the CBC after anchoring the alloying nanoparticles. The transmission electron microscopy (TEM) image of the PdCu/CBC in Fig. 1c displays homogeneous PdCu nanoparticles loaded onto the carbon support. The high-resolution TEM (HRTEM) image indicates that the lattice distance of an individual nanoparticle is 0.22 nm (inset in Fig. 1c), attributed to the (111) interplanar distance of the face-centred cubic (FCC) PdCu alloy,[33] and the HRTEM image of the nanoparticles located at different areas also shows the same results (Fig. S2, ESI†), confirming the formation of PdCu alloying nanoparticles on the CBC. For a
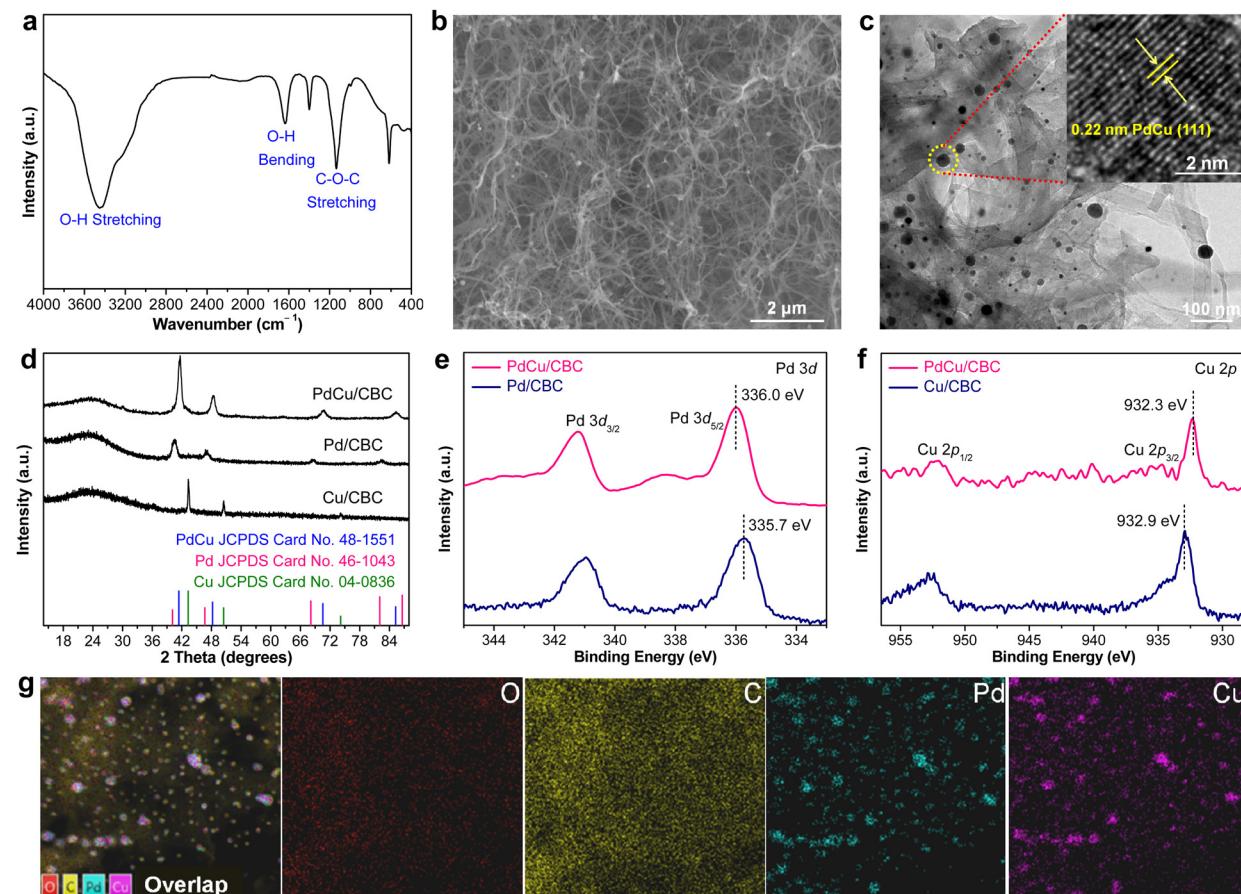
Fig. 1 (a) FT-IR spectrum of BC. (b) SEM and (c) TEM images of the PdCu/CBC. (d) XRD patterns of the Pd/CBC, Cu/CBC and PdCu/CBC. (e) Pd 3d XPS spectra of the Pd/CBC and PdCu/CBC. (f) Cu 2p XPS spectra of the Cu/CBC and PdCu/CBC. (g) Corresponding elemental mapping images of the PdCu/CBC.

meaningful comparison, Pd/CBC and Cu/CBC were also fabricated using a similar synthetic method to the PdCu/CBC except for only use of Pd^{2+} or Cu^{2+} as a precursor. Fig. S3 and S4 (ESI†) show the TEM images, elemental mapping images and X-ray photoelectron spectroscopy (XPS) analysis results of the Pd/CBC and Cu/CBC. To further confirm the formation of PdCu alloying nanoparticles on the CBC, the powder X-ray diffraction (XRD) measurements of the Pd/CBC, Cu/CBC and PdCu/CBC were performed, as shown in Fig. 1d. It can be clearly seen that the XRD patterns of the Pd/CBC, Cu/CBC and PdCu/CBC are consistent with the metallic Pd phase (JCPDS Card No. 46-1043), metallic Cu phase (JCPDS Card No. 04-0836) and PdCu alloying phase (JCPDS Card No. 48-1551), respectively.[34–36] Moreover, the XRD patterns of the PdCu/CBC are obviously different from those of the Pd/CBC and Cu/CBC samples. In this work, the XPS technique was also employed to investigate the chemical composition and chemical state of the Pd/CBC, Cu/CBC and PdCu/CBC. The high-resolution C 1s (Fig. S3c, S4c and S5b, ESI†) and O 1s (Fig. S3d, S4d and S5c, ESI†) XPS spectra confirm the presence of rich O groups and the formation of Pd–O, Cu–O and Pd/Cu–O bonds in the Pd/CBC, Cu/CBC and PdCu/CBC, respectively.[31,32] The high-resolution Pd 3d and Cu 2p XPS spectra were measured to analyze the electronic properties of PdCu alloy (Fig. 1e and f). Compared

to the sole Pd/CBC and Cu/CBC, the binding energy of Pd $3d_{5/2}$ for the Pd/CBC is located at ∼335.7 eV, while the binding energy of the PdCu/CBC is shifted slightly toward the high binding energy direction to ∼336.0 eV.[9,37] The binding energy of Cu $2p_{3/2}$ for the Cu/CBC is located at ∼932.9 eV, while a slight shift toward the low binding energy direction occurs for the PdCu/CBC (∼932.3 eV).[9,37] The above XPS results indicate the formation of PdCu alloy with favored internal electron transfer between Pd and Cu,[9,37] favourable for electrocatalysis. The elemental composition of the PdCu/CBC was further investigated by using energy-dispersive X-ray spectroscopy (EDX) (Fig. 1g) and inductively coupled plasma atomic emission spectrometry (ICP-AES) (Table S1, ESI†), and the obtained results suggest that the Pd to Cu molar ratio is about 1:1 for the PdCu/CBC. The corresponding elemental mapping images confirm that the Pd and Cu elements share similar distributions, implying the formation of PdCu alloying nanoparticles (Fig. 1g). The Brunauer–Emmett–Teller (BET) measurement indicates that the PdCu/CBC has a surface area of 162.4 $m^2 g^{-1}$ with microporous and mesoporous structures (Fig. S6, ESI†), which would be helpful for the exposure of catalytically active sites and mass transport during electrocatalysis.[31,32]

The as-fabricated PdCu/CBC electrocatalyst was subsequently evaluated for the electrocatalytic urea synthesis by

coupling NO_3^- and CO_2 under ambient conditions. All electrochemical measurements were performed in Ar- or CO_2-saturated 0.05 M KNO_3 electrolyte using an H-type two-compartment electrochemical cell, which was separated with a Nafion 211 membrane and equipped with three-electrode configurations (see the Experimental section for details, ESI†). Fig. 2a presents the linear sweep voltammetry (LSV) curves of the PdCu/CBC in CO_2- and Ar-saturated 0.05 M KNO_3 electrolytes. Interestingly, it was found that the current density was lowered by CO_2 feeding within the investigated potential range in comparison with that obtained in Ar-saturated electrolyte. In the Ar-saturated electrolyte, the obtained cathodic current densities at the given applied potentials could be ascribed to the NO_3^- reduction reaction (NO_3^-RR) and/or hydrogen evolution reaction (HER).[17] With the introduction of CO_2, the obviously decreased cathodic current densities at the given applied potentials could mean the effective inhibition of the NO_3^-RR and/or HER, thus facilitating the C–N coupling reaction for urea synthesis, consistent with recently

reported works.[17] To ensure the accuracy of the analysis data, we investigated in detail the reliability of the diacetyl monoxime colorimetric method and the ^{1}H nuclear magnetic resonance (^{1}H NMR) method for urea product determination in this work. The detailed experimental results and discussions are presented in Fig. S7–S12 (ESI†). The results demonstrate that during the electrocatalytic synthesis of urea, concurrently produced by-products such as NH_3 and NO_2^- have important influences on the measurement results of urea using the diacetyl monoxime colorimetric method (Fig. S8–S10, ESI†), consistent with the recently reported work by Wang et al.[21] In contrast, the influence of NH_3 and NO_2^- by-products is ignorable for the urea quantitative determination using the ^{1}H NMR method (Fig. S11 and S12, ESI†). Therefore, the ^{1}H NMR method was employed to qualitatively and quantitatively measure the produced urea in this work. The above experimental results could be helpful for other researchers to avoid possible false positive results of the urea measurement. As shown in Fig. S12b (ESI†), the ^{1}H NMR spectra of the products display three peaks
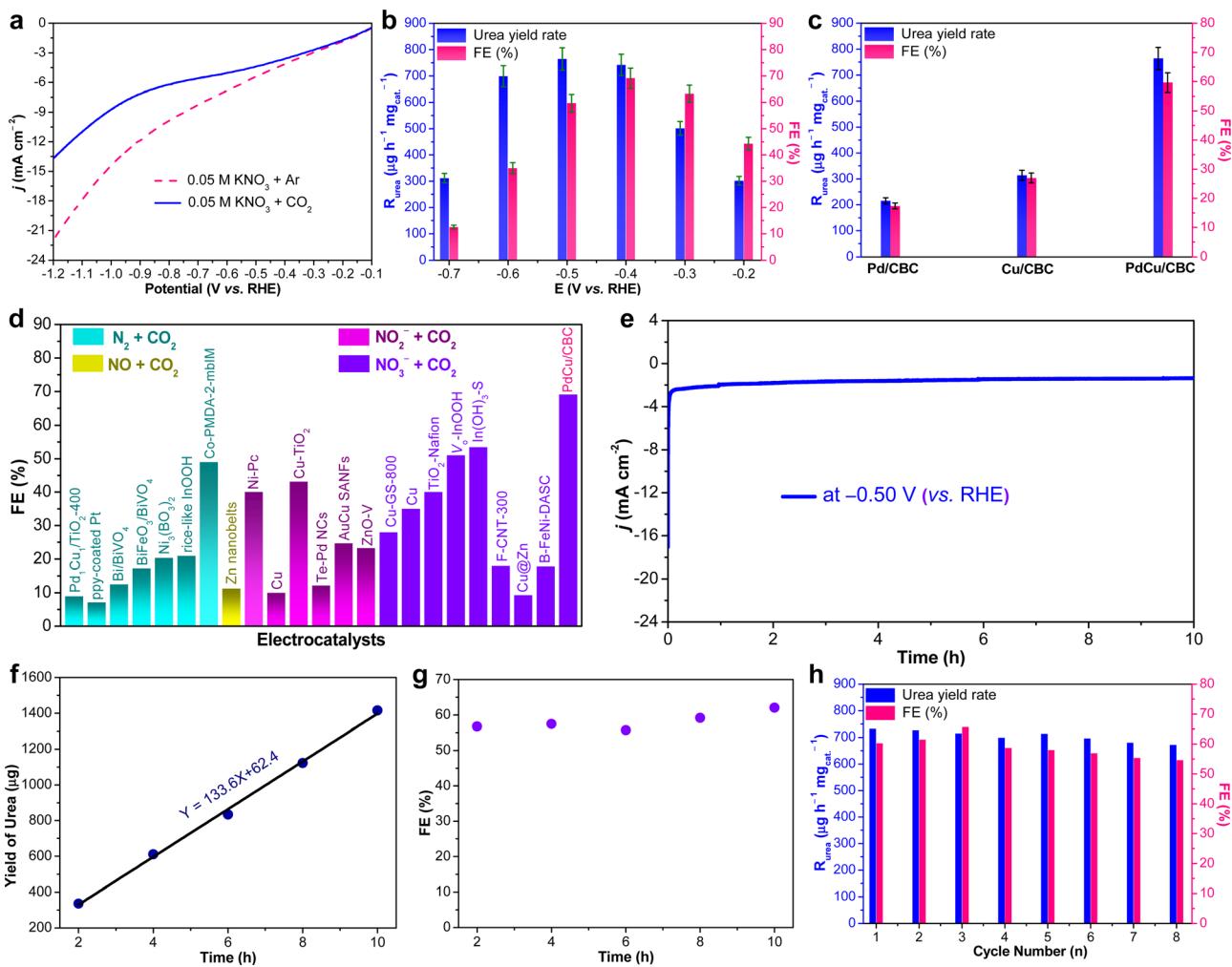
Fig. 2 (a) LSV curves of the PdCu/CBC in 0.05 M KNO_3 electrolyte with Ar or CO_2 feeding gas. (b) Dependence of R_{urea} and FE on the applied potentials. (c) R_{urea} and FE of the PdCu/CBC, Cu/CBC and Pd/CBC at −0.50 V (vs. RHE) for 2 h reaction. (d) Comparison of the FEs of the reported electrocatalysts and the PdCu/CBC with different nitrogen sources. (e) Stability test of the PdCu/CBC at −0.50 V (vs. RHE). (f) The urea yield and (g) FE for urea production over the PdCu/CBC toward electrochemical coupling NO_3^- with CO_2 with reaction time at −0.50 V (vs. RHE). (h) Recycling stability test of the PdCu/CBC.

identified as $^{14}NH_2CO^{14}NH_2$ ($\sim$5.6 ppm), d_6-DMSO (as an internal standard) ($\sim$2.5 ppm) and H_2O ($\sim$4.7 ppm), while no other liquid products can be detected, indicating the high selectivity of the PdCu/CBC toward urea synthesis through the C–N coupling reaction. Fig. 2b shows the dependence of the urea yield rate (R_{urea}) and faradaic efficiency (FE) on the applied potential in CO_2-saturated 0.05 M KNO_3 electrolyte over a 2 h period. The time-dependent current density curves at different potentials and the corresponding ^1H NMR spectra of the samples are shown in Fig. S12 (ESI†). The as-synthesized PdCu/CBC exhibits high electrocatalytic activity toward urea synthesis, affording a large R_{urea} of 763.8 $\pm$ 42.8 µg h^{-1} mg$_{cat.}$$^{-1}$ at −0.50 V ($vs.$ RHE) with a FE of 59.7 $\pm$ 3.4%. The highest FE that can be achieved was found to be 69.1 $\pm$ 3.8% at −0.40 V ($vs.$ RHE). In order to ensure the accuracy of the ^1H NMR results, the urease decomposition method was also adopted in this work (Fig. S13, ESI†). The quantitative analysis results based on the urease decomposition method demonstrate that the yielded urea is 785.2 $\pm$ 39.2 µg h^{-1} mg$_{cat.}$$^{-1}$, almost identical to that obtained from the NMR results. For a meaningful comparison, the Pd/CBC and Cu/CBC as electrocatalysts were also evaluated for urea synthesis. At −0.50 V ($vs.$ RHE) in CO_2-saturated 0.05 M KNO_3 electrolyte over a 2 h period, the R_{urea} and FE are 215.1 $\pm$ 11.8 µg h^{-1} mg$_{cat.}$$^{-1}$ and 17.4 $\pm$ 1.0% for the Pd/CBC and 314.2 $\pm$ 19.5 µg h^{-1} mg$_{cat.}$$^{-1}$ and 27.0 $\pm$ 1.7% for the Cu/CBC, respectively (Fig. 2c and Fig. S14, ESI†). The electrocatalytic performance of urea synthesis with CO_2 and NO_3^- exceeds those of most of the recently reported electrocatalysts of urea synthesis (Fig. 2d and Table S2, ESI†). Apparently, the PdCu/CBC displays far superior electrocatalytic urea synthesis performance, possibly owing to the existence of Pd and Cu dual sites with favored internal electron transferability. Besides the targeted urea product, the by-products NH_3, NO_2^-, CO and H_2 are inevitably produced during electrocatalysis, and also determined by the colorimetric methods and gas chromatography (GC) methods (Fig. S15–S18, ESI†). In contrast to the produced urea, the electrocatalytic activity toward the by-products NH_3 and NO_2^- is obviously lower, meaning a higher electrocatalytic selectivity of the PdCu/CBC toward urea synthesis. Meanwhile, no HCOOH or N_2H_4 product was detected during electrocatalysis (Fig. S12 and S19, ESI†). On the basis of the detected products during electrocatalytic urea synthesis, the faradaic efficiency (FE) of each electrocatalytic product at different potentials was calculated and is shown in Fig. S20 (ESI†). Obviously, the produced urea is the primary product at potentials from −0.20 V to −0.60 V ($vs.$ RHE), indicating a high selectivity of the PdCu/CBC toward urea synthesis. The stability test of the PdCu/CBC was conducted using CO_2-saturated 0.05 M KNO_3 electrolyte at −0.50 V ($vs.$ RHE) over a 10 h period (Fig. 2e). As shown, the obtained chronoamperometric curve displays an almost insignificant change in current density over the entire 10 h testing period (Fig. 2e). Significantly, the urea yield shows a good linear relationship with reaction time (Fig. 2f and Fig. S21, ESI†); moreover, the change in the corresponding FE is slight (Fig. 2g), signifying high stability of the PdCu/CBC for electrocatalytic urea synthesis. The cycling stability of the PdCu/CBC was examined using CO_2-saturated 0.05 M KNO_3 electrolyte

at −0.50 V ($vs.$ RHE) with a 2 h testing cycle for 8 consecutive cycles (Fig. S22, ESI†). As shown in Fig. 2h, the obtained R_{urea} and FE for 8 consecutive cycles show slight changes, demonstrating good cycling stability. The high stability of the PdCu/CBC can be attributed to its structural stability as evidenced by the XRD patterns, and TEM and elemental mapping images of the PdCu/CBC after 8 consecutive cycles (Fig. S23, ESI†). To confirm the produced urea that originated from the PdCu/CBC catalyzed coupling reaction of CO_2 with NO_3^-, the isotope labelling experiments were subsequently performed at −0.50 V ($vs.$ RHE) for 2 h measurement using CO_2-saturated 0.05 M $K^{14}NO_3$ and $K^{15}NO_3$ electrolytes. The ^1H NMR spectra in Fig. 3a indicate that the produced sample that originated from $^{14}NO_3^-$ shows a chemical shift at $\sim$5.59 ppm, consistent with the standard $^{14}NH_2CO^{14}NH_2$, while the $^{15}NO_3^-$ converted product displays chemical shifts at $\sim$5.48 and $\sim$5.70 ppm, completely consistent with the standard $^{15}NH_2CO^{15}NH_2$. These isotope labelling experimental results verify that the urea produced in this work is indeed from the PdCu/CBC catalyzed coupling reaction of CO_2 with NO_3^-. In addition, the quantitative analysis based on the ^1H NMR spectra of the standard $^{14}NH_2CO^{14}NH_2$ and $^{15}NH_2CO^{15}NH_2$ (Fig. S11 and S24, ESI†) was also carried out in this work. The experimental results demonstrate that using CO_2-saturated 0.05 M $K^{14}NO_3$ and $K^{15}NO_3$ electrolytes, the R_{urea} values of the yielded $^{14}NH_2CO^{14}NH_2$ and $^{15}NH_2CO^{15}NH_2$ are 763.8 $\pm$ 42.8 µg h^{-1} mg$_{cat.}$$^{-1}$ and 750.8 $\pm$ 34.3 µg h^{-1} mg$_{cat.}$$^{-1}$, respectively. As shown in Fig. 3b, the typical $^{14}NH_2CO^{14}NH_2$/$^{15}NH_2CO^{15}NH_2$ signal at 162.6 ppm is detectable for the electrolyte sample collected after 2 h electrocatalysis in ^{13}C NMR spectra. Furthermore, the typical $^{15}NH_2CO^{15}NH_2$ signal at 76.8 ppm is detectable for the electrolyte sample collected after 2 h electrolysis in ^{15}N NMR spectra (Fig. S25, ESI†). Thus, it can be concluded that the PdCu/CBC electrocatalyst exhibits high electrocatalytic activity toward ambient urea synthesis.

To eliminate the interferences of other factors on the produced urea, several controllable experiments were conducted as follows: (i) Ar-saturated 0.05 M KNO_3; (ii) CO_2-saturated 0.05 M KNO_3 without any applied potential (open-circuit); (iii) CO_2-saturated 0.05 M K_2SO_4 without any nitrogen-containing precursor; and (iv) carbon paper without the PdCu/CBC electrocatalyst. As shown in Fig. S26 (ESI†), only a negligible amount of urea product is detectable for all cases, further indicating that the produced urea is indeed from the electrocatalytic coupling reaction of CO_2 with NO_3^- on the PdCu/CBC. To illustrate that the PdCu/CBC exhibited enhanced C–N coupling activity, the as-synthesized PdCu alloy nanoparticles anchored on the conventional carbon black (denoted PdCu/CB) and carbonized bacterial cellulose (CBC) (denoted CBC) were also used as the electrocatalysts for the C–N coupling reaction (Fig. S27, ESI†). At −0.50 V ($vs.$ RHE) for 2 h, no urea product can be detected for the CBC, while the PdCu/CB shows a urea yield rate of 424.4 $\pm$ 24.6 µg h^{-1} mg$_{cat.}$$^{-1}$ and a FE of 33.3 $\pm$ 2.0% in CO_2-saturated 0.05 M KNO_3 electrolyte, apparently lower than those (763.8 $\pm$ 42.8 µg h^{-1} mg$_{cat.}$$^{-1}$ and 59.7 $\pm$ 3.4%, respectively) obtained from the PdCu/CBC (Fig. S27, ESI†). This is because the rich oxygen functional groups in the biomass-derived materials (*i.e.*, bacterial cellulose) have a superior coordination ability with
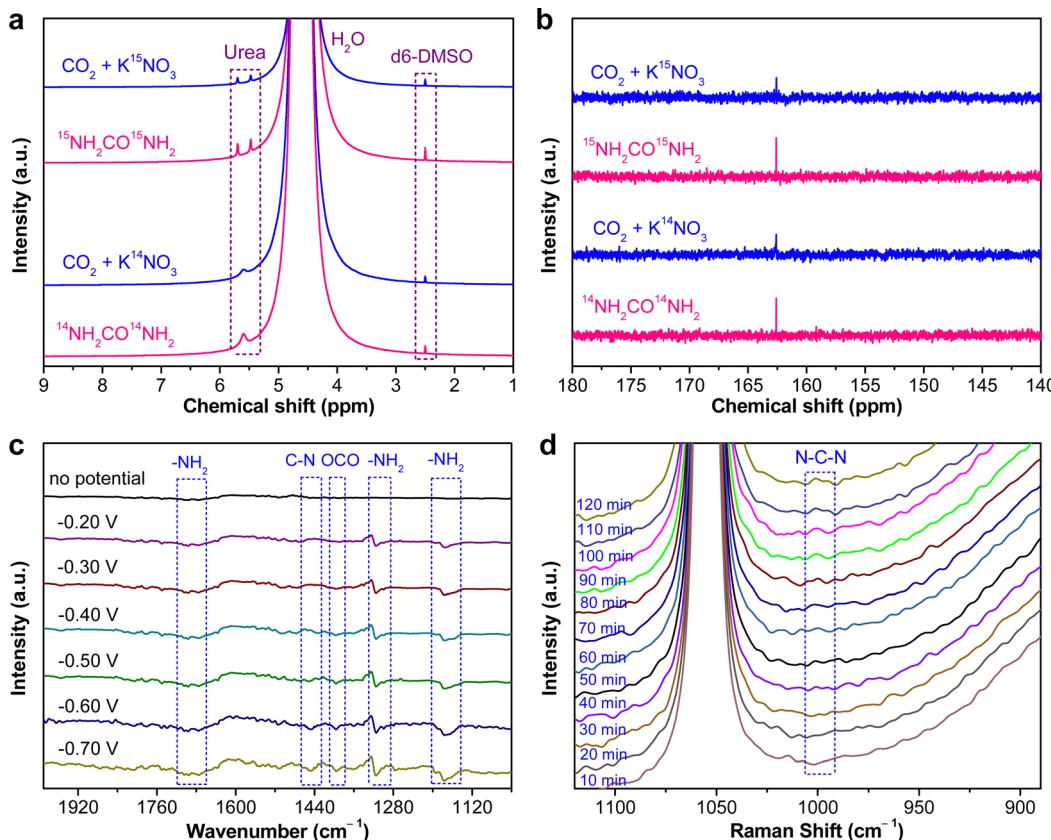
Fig. 3 (a) ^{1}H NMR spectra of 0.05 M $^{14}KNO_3$/$^{15}KNO_3$ electrolytes saturated with CO_2 after 2 h electrolysis and standard $^{14}NH_2CO^{14}NH_2$/$^{15}NH_2CO^{15}NH_2$ solutions. (b) ^{13}C NMR spectra of 0.05 M $^{14}KNO_3$/$^{15}KNO_3$ electrolytes saturated with CO_2 after 2 h electrolysis and standard $^{14}NH_2CO^{14}NH_2$/$^{15}NH_2CO^{15}NH_2$ solutions. (c) *Operando* SR-FTIR spectroscopy measurements under various potentials for the PdCu/CBC in CO_2-saturated 0.05 M KNO_3 electrolyte. (d) *Operando* Raman spectroscopy measurements of the PdCu/CBC in CO_2-saturated 0.05 M KNO_3 electrolyte at −0.50 V (*vs.* RHE) for 2 h reaction.

metal ions, which can be advantageously utilized to control the impregnation/loading of metal ions. More attractively, these chemically impregnated metal ions can be *in situ* converted to a nanoalloy anchored on the carbon support *via* M–O coordination configurations during the simple carbonization process. This unique oxygen coordination structure may be conducive to the adsorption and activation of CO_2 and NO_3^- to generate their corresponding active intermediates for facilitating the C–N coupling reaction.

To unveil the electrocatalytic activity mechanism of C–N coupling to urea, *operando* spectroscopic studies such as the advanced *operando* synchrotron radiation FTIR (SR-FTIR) and *operando* Raman measurements were performed to study the electrocatalytic urea synthesis by coupling CO_2 and NO_3^- on the PdCu/CBC over the potential range from −0.20 to −0.70 V (*vs.* RHE) in this work (Fig. S28 and S29, ESI†).[17] Fig. 3c shows the results of the SR-FTIR measurements. As shown, without the applied potential, there is no infrared absorption peak in the SR-FTIR spectra. In the investigated potential range, the infrared bands at ∼1685 and ∼1176 cm^{-1} are very obvious, which are attributed to the bending and rocking modes of –NH$_2$.[17,18,38] The wagging mode of –NH$_2$ is also found at ∼1317 cm^{-1}.[17,18,39] With the applied potential increasing from −0.20 to −0.40 V

(*vs.* RHE), a new weak vibration band at ∼1448 cm^{-1} appears, and its intensity is apparently increased with the potential further increasing from −0.40 to −0.70 V (*vs.* RHE), assignable to the stretching vibration of C–N.[17,18,38,40] The *operando* SR-FTIR results show that the urea synthesis by the electrocatalytic C–N coupling reaction of CO_2 with NO_3^- is successfully achievable, supportable for the electrocatalytic experimental results aforementioned. In addition, the infrared band belonging to *OCO* species adsorbed on the active sites appears at 1394 cm^{-1}, corresponding to its symmetric stretching mode.[17,18] Fig. 3d shows the *operando* Raman measurements for the electrocatalytic urea synthesis at −0.50 V (*vs.* RHE) for 2 h. The Raman intensity of the peak at around 1000 cm^{-1}, corresponding to the N–C–N stretching of urea, is increased obviously from 30 to 120 min, implying that the coupling reaction of CO_2 with NO_3^- takes place gradually with reaction time under the given electrocatalytic conditions.[41,42] The above *operando* SR-FTIR and Raman spectroscopy measurements confirm the successful realization of C–N coupling with CO_2 and NO_3^- over the PdCu/CBC in this work.

To deeply understand the intrinsic reason for the high electrocatalytic urea synthesis activity of the PdCu/CBC, we conducted the CO_2 temperature-programmed desorption (CO_2-TPD) experiments for PdCu/CBC and CBC samples.

As shown in Fig. 4a, the CBC substrate only shows a very weak CO_2 chemisorption peak at $\sim$255 °C, while the PdCu/CBC exhibits substantial enhancements in the CO_2 chemisorption at $\sim$360 and 436 °C, ascribed to the chemical adsorption of CO_2 on PdCu sites. As such, the binding strength of CO_2 chemisorption on the PdCu/CBC is remarkably stronger than that on the CBC, meaning the enhanced adsorption and activation of CO_2 on the PdCu/CBC for high-efficiency urea synthesis. To deeply understand the C–N coupling mechanism of the PdCu/CBC, the density functional theory (DFT) calculations were performed in this work. Fig. 4b shows the optimized structural model of PdCu alloy with an exposed (111) plane, and the Pd and Cu sites in PdCu alloy are the catalytically active centers for the adsorption and activation of CO_2 and NO_3^-, respectively. The Bader charge analysis shows that there is 1.65 e$^-$ charge transfer between Pd and Cu sites in the PdCu/CBC. The findings confirmed an apparent electron transfer between Cu and Pd for the formation of PdCu alloy, consistent with the XPS analysis. Such electron transfer changed the electronic states of metals and their d-band centers.[43,44] Fig. 4c shows the projected density of states (PDOS) of the Pd-4d or Cu-3d orbitals of

the PdCu/CBC, pristine Pd and pristine Cu. It was noted that under the same strain conditions, the d-band centers of pristine-Pd/Cu and Pd/Cu in the PdCu/CBC differed from each other. The d-band center value of Pd atoms in the PdCu/CBC was calculated to be −1.406 eV, showing an upshift in comparison with that (−1.819 eV) for pristine Pd. Similarly, the d-band center value of Cu atoms upshifted from −2.313 eV to −1.528 eV after the formation of PdCu alloy. This is due to the fact that the position of the d-band center is modulated by the electron distribution due to the charge transfer.[43,44] The increased d-band center value means that the PdCu nanoalloy can provide more d-bands to the adsorbate as compared with monometallic Pd or Cu, favoring the strong adsorption and activation of CO_2 and NO_3^- to generate their corresponding active intermediates for facilitating the C–N coupling reaction. Fig. 4d shows the free energy profile and reaction pathway of the C–N coupling on the PdCu(111) plane, and the optimized intermediate structure corresponding to each reaction step is displayed in Fig. S30 and S31 (ESI†). The electrocatalytic urea synthesis on PdCu is triggered by the thermodynamically spontaneous reduction reaction from HNO_3 to $*HNO_3$ with an energy output of
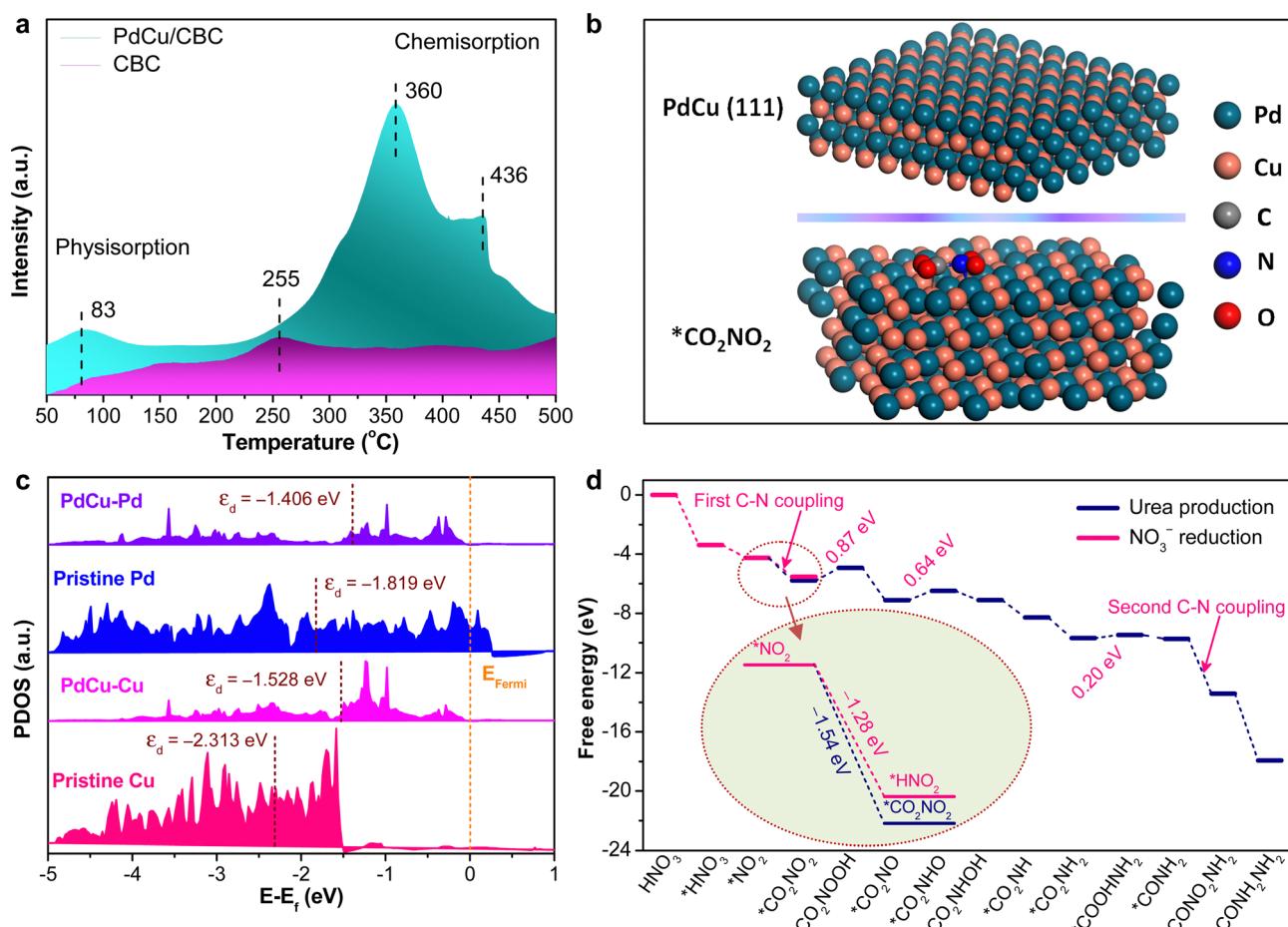

Fig. 4 (a) CO_2-TPD spectra of the PdCu/CBC and CBC. (b) DFT optimised configurations of the PdCu(111) plane and optimized geometric structure of the intermediate $*CO_2NO_2$ on PdCu(111). The green, orange, blue, red, white and grey balls represent Pd, Cu, N, O, H and C atoms, respectively. (c) The projected density of states (PDOS) onto the Pd-4d or Cu-3d orbitals of the PdCu/CBC, pristine Pd and pristine Cu. The dashed line represents the d-band center of Pd or Cu atoms. The Fermi level is set at 0 eV. (d) Free-energy diagram for urea production of the PdCu/CBC.

-3.38 eV. Then, *HNO$_3$ is further reduced to *NO$_2$ with an energy output of -0.87 eV. Moreover, we performed the calculations on *CO$_2$ conversion to *COOH or *CO on the PdCu(111) plane (Fig. S32, ESI†).[45] The results indicated that the corresponding kinetic energy barrier is 1.32 eV for the formation of *COOH on PdCu(111). Direct dissociation of CO$_2$ into adsorbed *CO and *O is unlikely to occur on the PdCu(111) plane due to the very large kinetic energy barrier of 2.82 eV. The further conversion of *COOH to *CO by breaking the strong C–O bond is also slow in kinetics, and the decomposition of *COOH to *CO + *OH encounters a large kinetic energy barrier of 1.32 eV. The elementary steps of hydrogenation of *CO$_2$ to *COOH and *COOH to *CO both have large energy barriers of ~ 1.3 eV. Importantly, it was found that the process from *NO$_2$ to *CO$_2$NO$_2$ with an energy output of -1.54 V is more thermodynamically favourable than the hydrogenation of *CO$_2$ to *COOH or *CO with an energy output of 1.3 eV (Fig. S32, ESI†) and the protonation of *NO$_2$ to *HNO$_2$ with an energy output of -1.28 V (inset in Fig. 4d and Fig. S33, ESI†), meaning more favored C–N coupling reaction with high selectivity. For the subsequent steps from *CO$_2$NO$_2$ to *CONH$_2$NH$_2$, most of the protonation processes are thermodynamically spontaneous; only three steps are uphill in energy, namely, the protonation of *CO$_2$NO$_2$ to *CO$_2$N-OOH with an uphill energy of 0.87 V, *CO$_2$NO to *CO$_2$NHO with an uphill energy of 0.64 V, and *CO$_2$NH$_2$ to *COOHNH$_2$ with an uphill energy of 0.20 V. Obviously, the protonation of *CO$_2$NO$_2$ to *CO$_2$NOOH could be the determining step for the overall urea production process.

Conclusions

In summary, we exemplified an adsorption-regulated synthetic strategy to fabricate PdCu alloying nanoparticles on carbonized bacterial cellulose (PdCu/CBC) for electrocatalytic synthesis of urea with CO$_2$ and NO$_3^-$ under ambient conditions. The results demonstrated that the as-synthesized PdCu/CBC provided Pd and Cu dual active sites with favored internal electron transferability, enabling adsorption and activation of CO$_2$ and NO$_3^-$ for high-efficiency electrocatalytic urea production under ambient conditions. Employing the PdCu/CBC electrocatalyst, the maximum urea yield rate achieved was found to be 763.8 ± 42.8 µg h^{-1} mg$_{cat.}^{-1}$ with a faradaic efficiency of 59.7 ± 3.4 at -0.50 V (vs. RHE) and high stability. The operando spectroscopy characterization studies combined with the theoretical calculations unveiled the catalytically active mechanisms of C–N coupling to generate urea with CO$_2$ and NO$_3^-$ through a coupling protonation process. The findings in this work would be helpful for the design and development of dual active site dominated electrocatalysts for high-efficiency C–N coupling to produce urea.

Author contributions

H. Zhang and S. Z. conceived the concept and designed the experiments. S. Z. and J. G. fabricated the catalysts and performed the material characterization and electrochemical

measurements. K. L. performed DFT calculations. Z. Z., M. J., W. L., Y. Y., G. W., Y. Z., H. Y. and H. Zhao contributed to the experimental design. H. Zhang and S. Z. co-wrote the manuscript. All authors discussed the results and commented on the manuscript.

Conflicts of interest

There are no conflicts to declare.

Acknowledgements

Notes and references

1 X. Zhu, X. Zhou, Y. Jing and Y. Li, Nat. Commun., 2021, **12**, 4080.
2 B. M. Comer, P. Fuentes, C. O. Dimkpa, Y.-H. Liu, C. A. Fernandez, P. Arora, M. Realff, U. Singh, M. C. Hatzell and A. J. Medford, Joule, 2019, **3**, 1578–1605.
3 C. Zhu, M. Wang, C. Wen, M. Zhang, Y. Geng, G. Zhu and Z. Su, Adv. Sci., 2022, **9**, 2105697.
4 M. Kitano, Y. Inoue, Y. Yamazaki, F. Hayashi, S. Kanbara, S. Matsuishi, T. Yokoyama, S.-W. Kim, M. Hara and H. Hosono, Nat. Chem., 2012, **4**, 934–940.
5 A. J. Martín, T. Shinagawa and J. Pérez-Ramírez, Chem, 2019, **5**, 263–283.
6 C. Chen, N. He and S. Wang, Small Sci., 2021, **1**, 2100070.
7 C. Zhu, C. Wen, M. Wang, M. Zhang, Y. Geng and Z. Su, Chem. Sci., 2022, **13**, 1342–1354.
8 D. B. Kayan and F. Köleli, Appl. Catal., B, 2016, **181**, 88–93.
9 C. Chen, X. Zhu, X. Wen, Y. Zhou, L. Zhou, H. Li, L. Tao, Q. Li, S. Du, T. Liu, D. Yan, C. Xie, Y. Zou, Y. Wang, R. Chen, J. Huo, Y. Li, J. Cheng, H. Su, X. Zhao, W. Cheng, Q. Liu, H. Lin, J. Luo, J. Chen, M. Dong, K. Cheng, C. Li and S. Wang, Nat. Chem., 2020, **12**, 717–724.
10 M. Yuan, J. Chen, Y. Bai, Z. Liu, J. Zhang, T. Zhao, Q. Wang, S. Li, H. He and G. Zhang, Angew. Chem., Int. Ed., 2021, **60**, 10910–10918.
11 M. Yuan, J. Chen, Y. Bai, Z. Liu, J. Zhang, T. Zhao, Q. Shi, S. Li, X. Wang and G. Zhang, Chem. Sci., 2021, **12**, 6048–6058.
12 M. Yuan, J. Chen, Y. Xu, R. Liu, T. Zhao, J. Zhang, Z. Ren, Z. Liu, C. Streb, H. He, C. Yang, S. Zhang and G. Zhang, Energy Environ. Sci., 2021, **14**, 6605–6615.
13 M. Yuan, J. Chen, H. Zhang, Q. Li, L. Zhou, C. Yang, R. Liu, Z. Liu, S. Zhang and G. Zhang, Energy Environ. Sci., 2022, **15**, 2084–2095.

14 M. Yuan, H. Zhang, Y. Xu, R. Liu, R. Wang, T. Zhao, J. Zhang, Z. Liu, H. He, C. Yang, S. Zhang and G. Zhang, *Chem. Catal.*, 2022, **2**, 309–3207.

15 D. B. Kayan and F. Köleli, *Appl. Catal., B*, 2016, **181**, 88–93.

16 D. Saravanakumar, J. Song, S. Lee, N. H. Hur and W. Shin, *ChemSusChem*, 2017, **10**, 3999–4003.

17 C. Lv, L. Zhong, H. Liu, Z. Fang, C. Yan, M. Chen, Y. Kong, C. Lee, D. Liu and S. Li, *Nat. Sustainability*, 2021, **4**, 868–876.

18 C. Lv, C. Lee, L. Zhong, H. Liu, J. Liu, L. Yang, C. Yan, W. Yu, H. H. Hng, Z. Qi, L. Song, S. Li, K. P. Loh, Q. Yan and G. Yu, *ACS Nano*, 2022, **16**, 8213–8222.

19 N. Meng, X. Ma, C. Wang, Y. Wang, R. Yang, J. Shao, Y. Huang, Y. Xu, B. Zhang and Y. Yu, *ACS Nano*, 2022, **16**, 9095–9104.

20 X. Liu, P. V. Kumar, Q. Chen, L. Zhao, F. Ye, X. Ma, D. Liu, X. Chen, L. Dai and C. Hu, *Appl. Catal., B*, 2022, **316**, 121618.

21 X. Wei, X. Wen, Y. Liu, C. Chen, C. Xie, D. Wang, M. Qiu, N. He, P. Zhou, W. Chen, J. Cheng, H. Lin, J. Jia, X.-Z. Fu and S. Wang, *J. Am. Chem. Soc.*, 2022, **144**, 11530–11535.

22 J. Leverett, T. Tran-Phu, J. A. Yuwono, P. Kumar, C. Kim, Q. Zhai, C. Han, J. Qu, J. Cairney, A. N. Simonov, R. K. Hocking, L. Dai, R. Daiyan and R. Amal, *Adv. Energy Mater.*, 2022, 2201500, DOI: **10.1002/aenm.202201500**.

23 T. Oshikiri, K. Ueno and H. Misawa, *Angew. Chem., Int. Ed.*, 2016, **55**, 3942.

24 X. Zhao, H. Yang, P. Jing, W. Shi, G. Yang and P. Cheng, *Small*, 2017, **13**, 1603279.

25 N. Cao, Y. Quan, A. Guan, C. Yang, Y. Ji, L. Zhang and G. Zheng, *J. Colloid Interface Sci.*, 2020, **577**, 109–114.

26 N. Meng, Y. Huang, Y. Liu, Y. Yu and B. Zhang, *Cell Rep. Phys. Sci.*, 2021, **2**, 100378.

27 S. Liu, S. Yin, Z. Wang, Y. Xu, X. Li, L. Wang and H. Wang, *Cell Rep. Phys. Sci.*, 2022, **3**, 100869.

28 X. Zhang, X. Zhu, S. Bo, C. Chen, M. Qiu, X. Wei, N. He, C. Xie, W. Chen and J. Zheng, *Nat. Commun.*, 2022, **13**, 1.

29 Y. Huang, R. Yang, C. Wang, N. Meng, Y. Shi, Y. Yu and B. Zhang, *ACS Energy Lett.*, 2022, **7**, 284–291.

30 J. Wang, L. Yu, L. Hu, G. Chen, H. Xin and X. Feng, *Nat. Commun.*, 2018, **9**, 1795.

31 S. Zhang, T. Shi, K. Li, Q. Sun, Y. Lin, L. R. Zheng, G. Wang, Y. Zhang, H. Yin and H. Zhang, *J. Phys. Chem. C*, 2022, **126**, 965–973.

32 S. Zhang, M. Jin, T. Shi, M. Han, Q. Sun, Y. Lin, Z. Ding, L. R. Zheng, G. Wang and Y. Zhang, *Angew. Chem., Int. Ed.*, 2020, **59**, 13423–13429.

33 Y. Qiu, L. Xin, Y. Li, I. T. McCrum, F. Guo, T. Ma, Y. Ren, Q. Liu, L. Zhou, S. Gu, M. J. Janik and W. Li, *J. Am. Chem. Soc.*, 2018, **140**, 16580–16588.

34 G.-T. Fu, X. Jiang, R. Wu, S.-H. Wei, D.-M. Sun, Y.-W. Tang, T.-H. Lu and Y. Chen, *ACS Appl. Mater. Interfaces*, 2014, **6**, 22790–22795.

35 Y. Zeng, P. X. Sun, Z. Pei, Q. Jin, X. Zhang, L. Yu and X. W. Lou, *Adv. Mater.*, 2022, **34**, 2200342.

36 H. Xu, H. Xu, Z. Chen, X. Ran, J. Fan, W. Luo, Z. Bian, W.-X. Zhang and J. Yang, *ACS Appl. Mater. Interfaces*, 2019, **11**, 3861–3868.

37 Q. Gao, H. S. Pillai, Y. Huang, S. Liu, Q. Mu, X. Han, Z. Yan, H. Zhou, Q. He, H. Xin and H. Zhu, *Nat. Commun.*, 2022, **13**, 2338.

38 R. Keuleers, H. O. Desseyn, B. Rousseau and C. Van Alsenoy, *J. Phys. Chem. A*, 1999, **103**, 4621–4630.

39 Y. Yao, S. Zhu, H. Wang, H. Li and M. Shao, *J. Am. Chem. Soc.*, 2018, **140**, 1496–1501.

40 M. Manivannan and S. Rajendran, *Int. J. Eng. Sci. Technol.*, 2011, **3**, 8048–8060.

41 R. L. Frost, J. Kristof, L. Rintoul and J. T. Kloprogge, *Spectrochim. Acta, Part A*, 2000, **56**, 1681–1691.

42 M. DelloStritto, M. L. Klein and E. Borguet, *J. Phys. Chem. A*, 2019, **123**, 5378–5387.

43 Q. Zhao, L. Liu, R. Liu and L. Zhu, *Chem. Eng. J.*, 2018, **353**, 311–318.

44 A. A. B. Padama, A. P. S. Cristobal, J. D. Ocon, W. A. Diño and H. Kasai, *J. Phys. Chem. C*, 2017, **121**, 17818.

45 X. Nie, X. Jiang, H. Wang, W. Luo, M. J. Janik, Y. Chen, X. Guo and C. Song, *ACS Catal.*, 2018, **8**, 4873.